QUANTUM COMPUTING

Quantum computational advantage using photons

Han-Sen Zhong[1,2]*, Hui Wang[1,2]*, Yu-Hao Deng[1,2]*, Ming-Cheng Chen[1,2]*, Li-Chao Peng[1,2], Yi-Han Luo[1,2], Jian Qin[1,2], Dian Wu[1,2], Xing Ding[1,2], Yi Hu[1,2], Peng Hu[3], Xiao-Yan Yang[3], Wei-Jun Zhang[3], Hao Li[3], Yuxuan Li[4], Xiao Jiang[1,2], Lin Gan[4], Guangwen Yang[4], Lixing You[3], Zhen Wang[3], Li Li[1,2], Nai-Le Liu[1,2], Chao-Yang Lu[1,2]†, Jian-Wei Pan[1,2]†

Quantum computers promise to perform certain tasks that are believed to be intractable to classical computers. Boson sampling is such a task and is considered a strong candidate to demonstrate the quantum computational advantage. We performed Gaussian boson sampling by sending 50 indistinguishable single-mode squeezed states into a 100-mode ultralow-loss interferometer with full connectivity and random matrix—the whole optical setup is phase-locked—and sampling the output using 100 high-efficiency single-photon detectors. The obtained samples were validated against plausible hypotheses exploiting thermal states, distinguishable photons, and uniform distribution. The photonic quantum computer, *Jiuzhang*, generates up to 76 output photon clicks, which yields an output state-space dimension of 10^{30} and a sampling rate that is faster than using the state-of-the-art simulation strategy and supercomputers by a factor of ~10^{14}.

The extended Church-Turing thesis is a foundational tenet in computer science, which states that a probabilistic Turing machine can efficiently simulate any process on a realistic physical device (*1*). In the 1980s, Feynman observed that many-body quantum problems seemed difficult for classical computers because of the exponentially growing size of the quantum-state Hilbert space. He proposed that a quantum computer would be a natural solution.

A number of quantum algorithms have since been devised to efficiently solve problems believed to be classically hard, such as Shor's factoring algorithm (*2*). Building a fault-tolerant quantum computer to run Shor's algorithm, however, still requires long-term efforts. Quantum sampling algorithms (*3*–*6*) based on plausible computational complexity arguments were proposed for near-term demonstrations of quantum computational speed-up, relative to current supercomputers, in solving certain well-defined tasks. If the speed-up appears overwhelming, such that no classical computer can perform the same task in a reasonable amount of time and this differential is unlikely to be overturned by classical algorithmic or hardware improvements, it is called quantum computational advantage or quantum supremacy (*7*, *8*). Here, we use the first term.

A recent experiment on a 53-qubit processor generated a million noisy (~0.2% fidelity) samples in 200 s (*8*), whereas a supercomputer would take 10,000 years. It was soon argued that the classical algorithm can be improved so that it would cost only a few days to compute all the 2^{53} quantum probability amplitudes and generate ideal samples (*9*). Thus, if the competition were to generate a much larger number of samples (for example, ~10^{10}), the quantum advantage would be reversed if there were sufficient storage. This sample size dependence of the comparison—an analog to loopholes in Bell tests (*10*)—suggests that quantum advantage would require long-term competitions between faster classical simulations and improved quantum devices.

Boson sampling, proposed by Aaronson and Arkhipov (*4*), was the first feasible protocol for quantum computational advantage. In boson sampling and its variants (*11*, *12*), nonclassical light is injected into a linear optical network, and the highly random, photon number– and path-entangled output state is measured by single-photon detectors. The dimension of the entangled state grows exponentially with both the number of photons and the modes, which quickly renders the storage of the quantum probability amplitudes impossible. The state-of-the-art classical simulation algorithm calculates one probability amplitude (Permanent of the submatrix) at a time. The Permanent is classically hard, and because at least one Permanent is evaluated for each sample (*13*, *14*), the sample size loophole can be avoided. In

[1]Hefei National Laboratory for Physical Sciences at Microscale and Department of Modern Physics, University of Science and Technology of China, Hefei, Anhui 230026, China. [2]CAS Centre for Excellence and Synergetic Innovation Centre in Quantum Information and Quantum Physics, University of Science and Technology of China, Shanghai 201315, China. [3]State Key Laboratory of Functional Materials for Informatics, Shanghai Institute of Microsystem and Information Technology, Chinese Academy of Sciences, Shanghai 200050, China. [4]Department of Computer Science and Technology and Beijing National Research Center for Information Science and Technology, Tsinghua University, Beijing 100084, China.
*These authors contributed equally to this work.
†Corresponding author. Email: cylu@ustc.edu.cn (C.-Y.L.); pan@ustc.edu.cn (J.-W.P.)

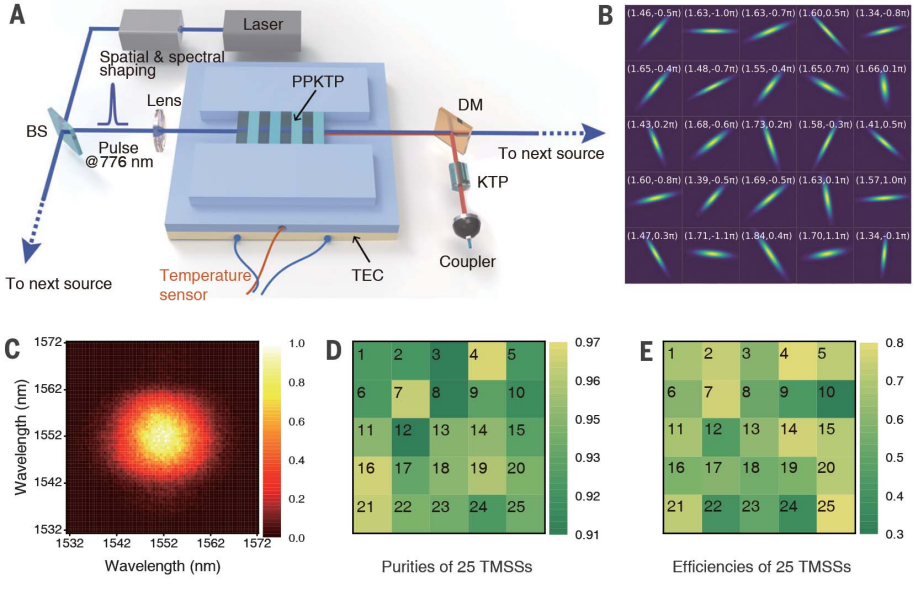

Fig. 1. Quantum light sources for Gaussian boson sampling (GBS). (**A**) An illustration of the experimental setup for generating squeezed states. A custom-designed laser system—consisting of a Coherent Mira 900, a pulse shaper, and a Coherent RegA 9000—generates the pump laser, which is spectrally and spatially shaped to reach transform limit (figs. S1 and S2). The pulsed laser is split by beamsplitters (BSs) into 13 paths (figs. S3 and S4) and focused onto 25 PPKTP crystals. Each crystal is placed on a thermo-electric cooler (TEC) for wavelength tuning. The downconverted photons are separated from the pumping laser by a dichromic mirror (DM); the time walk between different polarizations is compensated by a KTP crystal. (**B**) Wigner functions of all the 25 sources, showing the squeezing parameter r and phase ϕ of each source. In each subplot, the color encoding from purple to yellow represents a Wigner function from zero to its maximum. (**C**) The measured joint spectrum of the photon pairs indicates that the two photons are frequency-uncorrelated. (**D**) The purity of the 25 photon sources. The measured average purity is 0.938, obtained by unheralded second-order correlation measurement. (**E**) The measured collection efficiencies, with an average of 0.628.

addition, boson samplers use photons that can be operated at room temperature and are robust to decoherence.

Early proof-of-principle demonstrations of boson sampling (*15*, *16*) used probabilistic, post-selected pseudo–single photons from parametric downconversion (PDC) (*17*). Improved single-photon sources based on quantum dots were developed and were used to increase the multiphoton count rates, which culminated at 14-photon detection (*18*). However, scaling up boson sampling to a computationally interesting regime remained an outstanding experimental challenge.

Recently, Gaussian boson sampling (GBS) (*11*, *12*) has emerged as a new paradigm that not only can provide a highly efficient approach to large-scale implementations but also can offer potential applications in graph-based problems (*19*) and quantum chemistry (*20*). Instead of using single photons, GBS makes full use of the Gaussian nature of the PDC sources and uses single-mode squeezed states (SMSSs) as input nonclassical light sources, which can be deterministically prepared. Sending k SMSSs through an m-mode interferometer and sampling the output scattering events using threshold detectors (fig. S1), Quesada *et al.* showed that the output distribution is related to a matrix function called Torontonian (*12*), which is related to Permanent. Computing the Torontonian appears to be a computationally hard problem in the complexity class #P-hard. Li *et al*. recently showed that it takes about 2 days to evaluate a Torontonian function for a 50-photon click pattern (*21*).

Although small-scale demonstrations of GBS with up to five photons have been reported (*22*, *23*), implementing a large-scale GBS incurs technological challenges: (i) It requires arrays of SMSSs with sufficiently high squeezing parameters, photon indistinguishability, and collection efficiency. (ii) Large interferometers are needed with full connectivity, matrix randomness, near-perfect wave-packet overlap and phase stability, and near-unity transmission rate. (iii) In contrast to the Aaronson-Arkhipov boson sampling, where there is no phase relation between single photons, GBS requires phase control of all the photon number states in the SMSSs. (iv) High-efficiency detectors are needed to sample the output distribution. (v) The obtained sparse samples from a huge output state space should be validated, and the performance of the GBS should be benchmarked and compared with a supercomputer.

We start by describing the quantum light source arrays. Transform-limited laser pulses, with an average power of 1.4 W at a repetition rate of 250 kHz (figs. S1 and S2), are split into 13 paths and focused on 25 periodically poled potassium titanyl phosphate (PPKTP) crystals (Fig. 1A and figs. S3 and S4) to produce 25 two-mode squeezed states (TMSSs), which is equivalent to 50 SMSSs with a hybrid encoding (see below). The relative phase and squeezing parameter for each pair are shown in Fig. 1B. The PPKTP crystals are designed and temperature-controlled (fig. S5) to generate degenerate and frequency-uncorrelated photon pairs, as confirmed by the joint spectrum in Fig. 1C, which predicts a spectral purity of 0.98. The purity is increased to 0.99 by 12-nm filtering (figs. S6 and S7). A second estimation of the pairwise purity is by unheralded second-order correlation measurements (*24*). The measured purities are plotted in Fig. 1D, with an average of 0.938. The decrease of purity relative to the prediction from the joint spectra is mainly due to self–phase modulation. Figure 1E shows that the average collection efficiency is 0.628.

The whole optical setup—from the 25 PPKTPs to the 100-mode interferometer—must be locked to a fixed phase in the presence of various environmental perturbations. To achieve this aim, we developed an active phase-locking system (Fig. 2A) that covers the whole optical path, in combination with passive stabilization inside the interferometer (Fig. 2B) (*25*). For the active locking, the phase of the 776-nm laser is locked with a standard deviation of 0.04 rad [~5 nm (*25*)] (Fig. 2B, top). For the passive stabilization, the drift is controlled to be within λ/180 in 3.5 hours (Fig. 2B, bottom). For the whole system (Fig. 2D), the high-frequency noise standard deviation is λ/350 and the low-frequency drift is λ/63 within 1 hour, a time sufficient for completing the sampling and characterizations. We estimate that the drop in photon interference visibility as a result of the phase instability is less than 1%.

We made use of the photons' spatial and polarization degrees of freedom to realize a 100 × 100 unitary transformation (*15*, *26*). Here, the mode mapping is {1, 2, ... 100} = $\{|H\rangle_1|V\rangle_1|H\rangle_2|V\rangle_2 \ldots |H\rangle_{50}|V\rangle_{50}\}$, where H and V denote horizontal and vertical polarization, respectively, and the subscripts denote the spatial mode in the interferometer. We developed a compact three-dimensional design for the 50–spatial mode interferometer, which

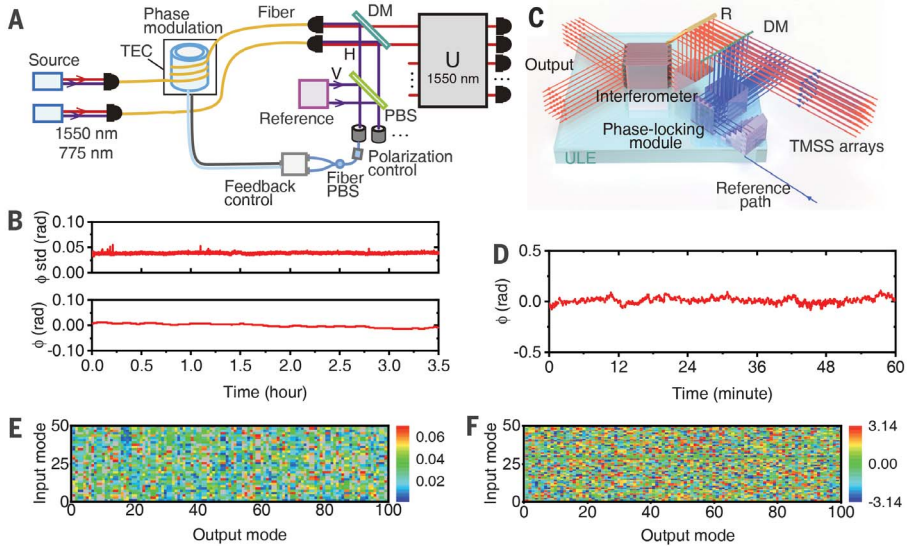

Fig. 2. Phase locking from the photon sources to the interferometer. (**A**) Schematic diagram of the active phase-locking system. A pump laser beam is used as a reference for all the squeezed states. After propagating through a ~2-m free space and 20-m optical fiber, a ~10-μW pump laser that shares the same propagation path as the downconverted photons is separated by a dichromatic mirror; The pump laser pulses are then combined on a beamsplitter with the reference laser pulse. A balanced detection scheme, which is insensitive to laser power fluctuation, is used to read out the phase information. To overcome the path length fluctuation, we wind optical fiber (length 5 m) around a piezoelectric cylinder with sensitivity of 1.5 rad/V, resonance frequency of 18.3 KHz, and dynamical range of 300 rad. (**B**) Phase stability tests. The top and bottom panels respectively show a typical monitoring of phase fluctuation of active and passive phase locking over 3.5 hours. The measured standard deviation of the phase is as small as 0.02 rad (λ/150) for active phase locking and 0.017 rad (λ/180) for passive phase locking. (**C**) We apply passive phase stabilization to the interferometer by adhering the devices onto an ultralow-expansion glass plate that is temperature-stabilized within 0.02°C. The blue light paths are for the interference of the 25 pumping lasers with the reference laser. The red light paths are the input and output of the photonic network. R denotes a reflective mirror. (**D**) A typical phase stability measurement of the whole system in 1 hour. (**E**) Diagram of the measured 5000 amplitudes of the matrix. (**F**) Diagram of the measured 5000 phases of the matrix.

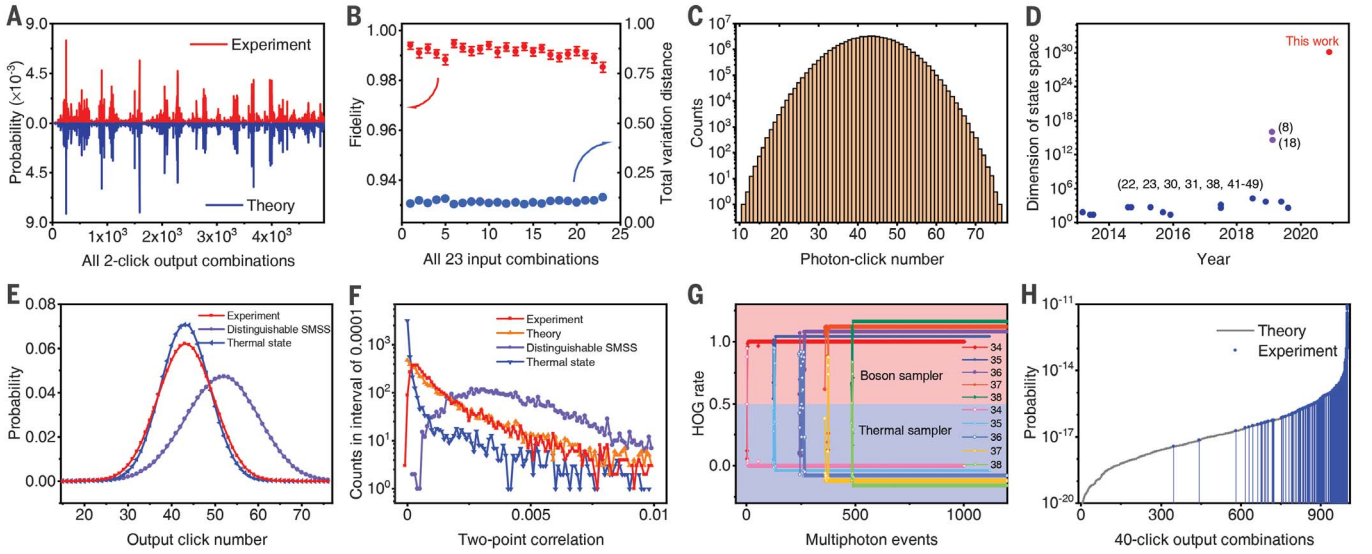

Fig. 3. Experimental validation of the GBS setup. (**A**) Experimental (red) and theoretical (blue) two-photon distribution with three TMSSs input. (**B**) Summary of statistical fidelity and total variation distance of two-photon distribution for 23 different input sets. (**C**) Output photon number distribution with all 25 TMSSs input. The average detected photon number is 43; the maximal detected photon number is 76. (**D**) Summary of the output state-space dimension. (**E**) Photon number distributions of the experimental result (red) and from the thermal state (blue) and distinguishable SMSS (purple) hypotheses. The deviations of the line shape and peak positions indicate that our experiment is far from these two hypotheses. (**F**) Two-photon correlation statistics for all two-mode combinations. The statistic of the experimental results (red) highly overlap with the theoretical predictions (orange) and deviate from the thermal state hypothesis (blue) and the distinguishable SMSS hypothesis (purple). (**G**) Validation against thermal state hypothesis with detected photon number ranging from 34 to 38. (**H**) Validation against uniform distribution.

simultaneously fulfills near-perfect phase stability and wave-packet overlap, full connectivity, random matrix, and near-unity transmission rate (Fig. 2C) (*25*). This optical network effectively consists of 300 beamsplitters and 75 mirrors (see fig. S9). The transmission rate of the interferometer is measured to be 97.7%, and the average coupling efficiency in all the output ports is ~90%. We estimate that the mode mismatch causes a ~0.2% drop of the interference visibility between independent photons.

Contrary to the Aaronson-Arkhipov boson sampling, where the sampling matrix is given solely by the interferometer, the GBS matrix absorbs both the unitary transformation of the interferometer and the squeezing parameters and phases of the Gaussian input state. We reconstructed the corresponding unitary matrix of the spatial polarization hybrid-encoded 100 × 100 interferometer, as plotted in Fig. 2, E and F, for the elements of amplitudes and phases, respectively. Further analysis shows that the obtained matrix is unitary (fig. S14) and Haar-random (fig. S15).

We named our GBS machine *Jiuzhang*. We first describe the experimental results from the easy regime, where we can obtain the full output distribution. We tested with three pairs of input TMSSs and two-photon click in the output. The obtained distribution is plotted in Fig. 3A. We use fidelity (F) and total variation distance (D) to characterize the obtained distribution, defined by $F = \sum_i \sqrt{p_i q_i}$, and $D = \sum_i |p_i - q_i|/2$ (p_i and q_i denote the theoretical and experimental probability of the ith basis, respectively). For a perfect boson sampler, the fidelity should equal 1 and the distance should be 0. The measured average fidelity is 0.990 ± 0.001, and the measured average distance is 0.103 ± 0.001. The data for all 23 different input configurations are shown in Fig. 3B, which confirms that the GBS works properly.

We next consider the sparse and intractable regime. Using 25 TMSSs as input, the output photon number distribution using threshold detectors is plotted in Fig. 3C. The average click number is 43. Within 200 s, we obtained 3,097,810 events of 43-photon coincidence, and one 76-photon coincidence. The state-space dimension of our experiment is plotted in Fig. 3D, reaching up to 10^{30}, which is 14 and 16 orders of magnitude larger than the dimension achieved in previous experiments using superconducting qubits (*8*) and single photons (*18*), respectively.

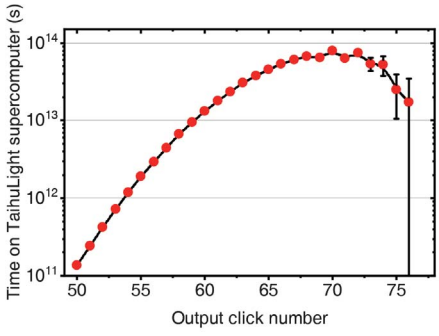

Fig. 4. Classical computational cost. The estimated time cost on a Sunway TaihuLight supercomputer is plotted as a function of the output photon click number. The error bar is calculated from Poissonian counting statistics of the raw detected events.

Although a full verification of the results in the large–photon number regime is unlikely because of the nature of the sampling problem, we hope to provide strong evidence that the large-scale GBS continues to be governed by quantum mechanics when it reaches the quantum advantage regime. The credibility of the certification processes (*27*–*32*) relies on gathering circumstantial evidence while ruling out alternative hypotheses that might be plausible in this experiment. We validated the desired input TMSSs against input photons that are thermal states (which would result from excessive photon loss) and are distinguishable (which would be caused by mode mismatch).

We began by comparing the obtained output distribution with the hypotheses using thermal light and distinguishable SMSSs. Figure 3E shows evidently strong deviations in line shapes and peak positions, which imply that the obtained distribution indeed arises from genuine multiphoton quantum interference. We then investigated two-point correlation (*32*), which is derived from the Hanbury-Brown-Twiss experiment, to reveal the nonclassical

properties of the output light field. Here, the two-point correlation between mode i and mode j is defined as $C_{i,j} = \langle \Pi_1^i \Pi_1^j \rangle - \langle \Pi_1^i \rangle \langle \Pi_1^j \rangle$, where $\Pi_1^i = \mathbf{I} - |0\rangle_i \langle 0|_i$ represents a click in mode i. We calculated the distribution of all values of $C_{i,j}$ for the experimentally obtained samples, and then compared the result with those from theoretical predictions, the thermal-states hypothesis, and the distinguishable-SMSSs hypothesis. As shown in Fig. 3F, the statistics of experimental samples diverge from the two hypotheses and agree with the theoretical prediction.

Having studied the whole distribution, we closely looked into each subspace with a specific photon click number. We developed a method called the heavy output generation (HOG) ratio test (*25*). Figure 3G and fig. S26 show typical examples of HOG analysis for photon clicks from 26 to 38, which show a stark difference between TMSSs with thermal states. We emphasize that the tested 26- to 38-click regime—which shares the same setup as higher photon number—is in the post-selected subspace that effectively suffers from more photon loss than in the regime with a larger number of clicks, which we deduce can be validated against the thermal-states hypothesis with higher confidence.

We continue to rule out another important hypothesis that boson sampling output would be operationally indistinguishable from a uniform random outcome, one of the earliest criticisms (*27*) of boson sampling. In stark contrast, because of constructive and destructive interference, an ideal boson sampler is expected to generate samples with lognormal-like distribution (*4*, *27*). We developed a method (*25*) to reconstruct the theoretical probability distribution curve for the 40-photon case (Fig. 3H). We can match each obtained sample to the theoretical curve, as illustrated by the blue data points and vertical blue lines in Fig. 3H (see fig. S27 for more data). The frequency of occurrence of the blue lines is in good agreement with the probability curve, which intuitively indicates that our results cannot be reproduced by a uniform sampler.

Finally, we estimated the classical computational cost to simulate an ideal GBS device. We have benchmarked the GBS on the Sunway TaihuLight supercomputer (*21*) using a highly optimized algorithm (*33*). The time cost to calculate one Torontonian scales exponentially as a function of output photon clicks. Moreover, to obtain one sample usually requires the calculation of ~100 Torontonians of the candidate samples (*13*). The GBS simultaneously generates samples of different photon-number coincidences (Fig. 3C), which can be seen as a high-throughput sampling machine. For each output channel and the registered counts in Fig. 3C, we calculated the corresponding time cost for the supercomputer (Fig. 4). Summing over the data points in Fig. 4, we estimate that the required time cost for the TaihuLight to generate the same number of samples in 200 s with the GBS device would be 8×10^{16} s, or 2.5 billion years. For the Fugaku supercomputer, the time cost would be 2×10^{16} s, or 0.6 billion years. We hope that this work will inspire new theoretical efforts to quantitatively characterize large-scale GBS, improve the classical simulation strategies optimized for the realistic parameters (*33*, *34*), and challenge the observed quantum computational advantage of ~10^{14}.

REFERENCES AND NOTES

1. E. Bernstein, U. Vazirani, in *Proceedings of the 25th Annual ACM Symposium on Theory of Computing* (1993).
2. P. W. Shor, in *Proceedings of the 35th Annual Symposium on Foundations of Computer Science* (1994).
3. B. M. Terhal, D. P. DiVincenzo, arXiv 0205133 [quant-ph] (11 March 2004).
4. S. Aaronson, A. Arkhipov, in *Proceedings of the 43rd Annual ACM Symposium on Theory of Computing* (2011).
5. S. Aaronson, L. Chen, in *Proceedings of the 32nd Computational Complexity Conference* (2017).
6. M. J. Bremner, A. Montanaro, D. J. Shepherd, *Phys. Rev. Lett.* **117**, 080501 (2016).
7. J. Preskill, Rapporteur talk at the 25th Solvay Conference on Physics, Brussels (2012).
8. F. Arute *et al*., *Nature* **574**, 505–510 (2019).
9. E. Pednault, J. A. Gunnels, G. Nannicini, L. Horesh, R. Wisnieff, arXiv 1910.09534 [quant-ph] (22 October 2019).
10. A. W. Harrow, A. Montanaro, *Nature* **549**, 203–209 (2017).
11. C. S. Hamilton *et al*., *Phys. Rev. Lett.* **119**, 170501 (2017).
12. N. Quesada, J. M. Arrazola, N. Killoran, *Phys. Rev. A* **98**, 062322 (2018).
13. A. Neville *et al*., *Nat. Phys.* **13**, 1153–1157 (2017).
14. P. Clifford, R. Clifford, in *Proceedings of the 29th Annual ACM-SIAM Symposium on Discrete Algorithms* (2018).
15. M. A. Broome *et al*., *Science* **339**, 794–798 (2013).
16. J. B. Spring *et al*., *Science* **339**, 798–801 (2013).
17. P. G. Kwiat *et al*., *Phys. Rev. Lett.* **75**, 4337–4341 (1995).
18. H. Wang *et al*., *Phys. Rev. Lett.* **123**, 250503 (2019).
19. J. M. Arrazola, T. R. Bromley, *Phys. Rev. Lett.* **121**, 030503 (2018).
20. J. Huh, G. G. Guerreschi, B. Peropadre, J. R. McClean, A. Aspuru-Guzik, *Nat. Photonics* **9**, 615–620 (2015).
21. X. Li *et al*., arXiv 2009.01177 [cs.DC] (2 September 2020).
22. H.-S. Zhong *et al*., *Sci. Bull.* **64**, 511–515 (2019).
23. S. Paesani *et al*., *Nat. Phys.* **15**, 925–929 (2019).
24. A. Christ, K. Laiho, A. Eckstein, K. N. Cassemiro, C. Silberhorn, *New J. Phys.* **13**, 033027 (2011).
25. See supplementary materials.
26. I. Dhand, S. K. Goyal, *Phys. Rev. A* **92**, 043813 (2015).
27. S. Aaronson, A. Arkhipov, *Quantum Inf. Comput.* **14**, 1383 (2014).
28. M. C. Tichy, K. Mayer, A. Buchleitner, K. Mølmer, *Phys. Rev. Lett.* **113**, 020502 (2014).
29. M. Walschaers *et al*., *New J. Phys.* **18**, 032001 (2016).
30. N. Spagnolo *et al*., *Nat. Photonics* **8**, 615–620 (2014).
31. J. Carolan *et al*., *Nat. Photonics* **8**, 621–626 (2014).
32. D. S. Phillips *et al*., *Phys. Rev. A* **99**, 023836 (2019).
33. N. Quesada, J. M. Arrazola, *Phys. Rev. Res.* **2**, 023005 (2020).
34. H. Qi, D. J. Brod, N. Quesada, R. García-Patrón, *Phys. Rev. Lett.* **124**, 100502 (2020).

ACKNOWLEDGMENTS

This work is dedicated to the people in the fight against the COVID-19 outbreak, during which the final stage of this experiment was carried out. We thank J. Renema, J. P. Dowling, C. Weedbrook, N. Quesada, Y. Jiang, J.-W. Jiang, S.-Q. Gong, B.-B. Wang, Y.-H. Li, H.-W. Cheng, Q. Shen, Y. Cao, Y. Chen, H. Lu, H. Fu, and T.-Y. Chen for very helpful discussions and assistance. **Funding:** Supported by the National Natural Science Foundation of China, the National Key R&D Program of China, the Chinese Academy of Sciences, the Anhui Initiative in Quantum Information Technologies, and the Science and Technology Commission of Shanghai Municipality. **Author contributions:** C.-Y.L. and J.-W.P. designed and supervised the research. H.-S.Z., M.-C.C., and J.Q. developed the theory. H.-S.Z., H.W., Y.-H.D., L.-C.P., Y.-H.L., J.Q., D.W., X.D., L.L., N.-L.L., and C.-Y.L. carried out the optical experiment and collected the data. Y.H. and X.J. designed the 100-channel counter. M.-C.C., Y.L., P.H., L.G., and G.Y. performed data analysis and validation on a supercomputer. P.H., X.-Y.Y., W.-J.Z., H.L., L.Y., and Z.W. developed single-photon detectors. H.-S.Z., M.-C.C., C.-Y.L., and J.-W.P. analyzed the data and prepared the manuscript. All authors discussed the results and reviewed the manuscript. **Competing interests:** The authors declare no competing interests. **Data and materials availability:** All data are available in the manuscript or the supplementary materials.

SUPPLEMENTARY MATERIALS

science.sciencemag.org/content/370/6523/1460/suppl/DC1
Materials and Methods
Supplementary Text
Figs. S1 to S28
Tables S1 to S3
References (*35*–*50*)

19 September 2020; accepted 19 November 2020
Published online 3 December 2020
10.1126/science.abe8770